

Motion Sensorless IPMSM Control Using Linear Moving Horizon Estimation With Luenberger Observer State Feedback

Andreas Andersson^{ID}, *Student Member, IEEE*, and Torbjörn Thiringer, *Senior Member, IEEE*

Abstract—This paper presents an investigation of motion sensorless control based on the frame work of moving horizon estimation (MHE), validated experimentally with a rear axle electrical drive unit used in automotive applications. Both steady-state performance and dynamic performance, including speed reversal, are investigated. In addition, a well-established active flux-based observer is implemented and referenced to objectively evaluate the proposed MHE. It is shown that the proposed solution is feasible, that the associated dynamic optimization problem can be solved in real time, while exploiting the attractiveness of the approach to obtain highly accurate estimates. Moreover, the absence of d -axis flux in the proposed solution is considered a significant strength. Conclusively, it turns the proposed solution into a universal solution for any synchronous motor, regardless of whether a PM, PM-assisted, or reluctance motor is used, nondependent on the presence of magnetic saliency.

Index Terms—Electric drives, moving horizon estimation (MHE), permanent magnet synchronous machine (PMSM), sensorless control.

I. INTRODUCTION

PERMANENT magnet synchronous machines (PMSMs) are widely used in industrial applications due to their high energy efficiency and high power and torque density capabilities [1], [2]. A typical application is within the field of automotive applications as propulsion machines in electric and hybrid-electric vehicles—an application where energy efficiency and torque density, for obvious reasons, are important key figures. For such applications, the need of accurate and reliable rotor position information is twofold. First, it is needed to enable specific system attributes such as high-performance closed-loop control systems. Second, it is essential to fulfill functional safety requirements. Such functional safety requirements, originating from the standard ISO-26262 and automotive safety integrity levels, can include, but is not limited to, system stability criteria, fault handling abilities, and output torque tracking abilities.

Manuscript received September 15, 2017; revised November 16, 2017; accepted December 26, 2017. Date of publication January 8, 2018; date of current version June 6, 2018. This work was supported in part by Swedish Energy Agency and in part by Volvo Car Group. (Corresponding author: Andreas Andersson.)

A. Andersson is with the Department of Electrical Propulsion Systems, Volvo Car Group, SE-41878 Gothenburg, Sweden (e-mail: andreas.andersson.6@volvocars.com).

T. Thiringer is with the Department of Electric Engineering, Chalmers University of Technology, SE-41258 Gothenburg, Sweden (e-mail: torbjorn.thiringer@chalmers.se).

Digital Object Identifier 10.1109/TTE.2018.2790709

Despite the inherent difficulties with sensorless control, there exist intermediate options where a software-based estimator, for instance, can act as a complement to the existing sensor. Either for redundancy purposes or as complement to a low-speed, low-resolution, and low-cost sensor. Options that according to [3] motivate the need for further research within the area, which also is emphasized.

Methods for sensorless control of ac drives have been extensively researched the last decades [3]–[7]. Typically, researchers divide the methods into two categories—methods based on high-frequency (HF) signal injection and methods using the fundamental electrical frequency, often referred to as the fundamental model-based methods [8]–[11].

The objective of model-based methods is to use mathematical models to enable access to unknown information based on available information. Naturally, options for different system model representations, application specific limitations, and solution approaches give rise to a vast amount of proposed solutions in the literature, neatly illustrated in [4], [5], [7], [11], and [12].

In [3], an extensive analysis on solutions specifically intended for salient-pole PMSM is given, and prospects for application areas are discussed. Sul *et al.* [3] highlight applications with heavily saturated, high power density, interior PMSM (IPMSM) as a developing area for sensorless control. Applications suffering from severe operation conditions and significant parameter variations.

In [4], active flux, model-based, observers were thoroughly investigated showing their strong potential. Moreover, the machine topology universality and the notable simplifications possible as a result of the use of active flux are also shown and discussed.

Moving horizon estimation (MHE), which is the topic of this paper, has been successfully researched previously for different applications. Frick *et al.* [13] determined its superiority to more established conventional estimator techniques, such as model reference adaptive system- and extended Kalman filter (EKF)-based observers, for sensorless induction motor drives. Kuhl *et al.* [14] reported on the superiority of MHE compared to EKF-based observers in chemical engineering problems. Yet, to the authors knowledge, MHE-based estimators for sensorless control of synchronous machines have not been researched.

In this paper, the authors propose a robust active flux-based MHE with a Luenberger preestimator for automotive

TABLE I

PMSM PARAMETERS AT $T = 22^\circ\text{C}$ AND AT RATED TORQUE AND SPEED

Variable	Value
Number of pole pairs	5
L_d	183 [μH]
L_q	416 [μH]
λ_m	48.1 [mWb]
R_s	13.2 [m Ω]
Number of slots	45
Number of parallel branches	5
Iron Material	M270-35A

applications. The investigated machine is an IPMSM with v-shaped magnet placement and significant saliency. The MHE approach relies on a series of measurements, observed over a horizon with fixed length. At each time instance, the series of measurements forward simulation of a system model and constraints are used to define a cost function. A function which is defined by a set of weighted least squares. The optimization objective is to minimize the cost function, subjected to the given constraints. As decision variables, the algorithm estimates the nonmeasured system states and the process noise for each time instance across the horizon.

At every iteration, the horizon is shifted forward in time, continuously adding new data to the MHE problem. Data falling out of the horizon at every time shift of the horizon are summarized in an arrival cost to enhance the performance. The Luenberger preestimator was used to further enhance the performance. Primarily at low rotational speeds.

The main contribution of this paper is to demonstrate the abilities model-based prediction has in the fields of sensorless control of electrical machines. The experimental results show its feasibility in real-time implementations with high update frequencies and time-varying systems.

It is of importance to emphasize the proposed methods inherent robustness to parameter variations. Explicitly, only the stator resistance and the quadrature-axis inductance are affecting the performance of the estimator, where the effects of stator resistance variations are only minor.

II. METHOD

The machine used in this investigation is a single-barrier IPMSM with v-shaped permanent magnet placement. The application of the investigated machine is hybrid-electric vehicle propulsion.

The machine, parametrized in Table I, was controlled using a real-time implementation of the discrete-time controller using a 2.8-GHz multicore processor and field-programmable gate array-based I/O. The control system was updated synchronously with the pulsewidth modulation triangular wave at a frequency of 8 kHz. In Fig. 1, the experimental setup is shown together with a cross section view of the investigated machine.

With a dc-voltage of 220 V and peak phase current of 150 A, the rated speed and torque were approximately 3700 r/min and 65 Nm, respectively.

For all results originating from the experimental testing, the rotor position estimate is used in closed-loop throughout

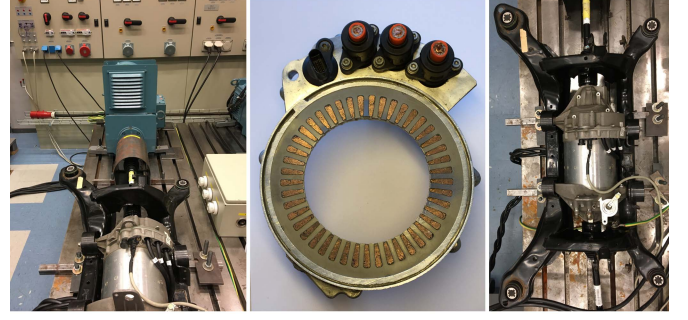


Fig. 1. Photograph of the experimental setup (left and right) and cross section of the investigated machine (middle).

the control system. Both for the rotational speed estimate and dq coordinate system orientation.

III. THEORY

A. Discrete-Time Linear State Space Model of IPMSM

The sensorless solution proposed in this paper is based on the concept of active flux, also known as torque producing flux. A concept which, to the best of the authors knowledge, first was introduced by Boldea *et al.* [5]. Note similarities and differences to previously researched extended electromotive force (EMF) solutions [4]. The active flux concept renders salient-pole ac machines into mathematically nonsalient ac machines. Observers originating from this concept have been extensively researched, both for different machine topologies and applications. Different derivatives of active flux-based observers can be found in the literature, for instance in [5] and in [15]. The concept of active flux is based on the appearance of the active flux vector in stationary coordinates, which by its definition falls along the d -axis of the machine, if cross-saturation is either absent or compensated for [16]. Intuitively, it makes a good basis for rotor position estimation.

The active flux is defined as the flux, which multiplied with the q current, produces torque. For a PM synchronous machine, using dq coordinates, it is defined as

$$\lambda_d^a = \lambda_m + (L_d - L_q)i_d \quad (1)$$

where λ_d^a , λ_m , L_d , and L_q are the active flux, the permanent magnet flux constant, and the d -axis and q -axis inductances, respectively. i_d is the momentary d -axis current.

From the dq representation of the salient pole machine, the following nonsalient model can be obtained [5]:

$$u_s = R_s i_s + (p + j\omega)L_q i_s + (p + j\omega)\lambda_d^a \quad (2)$$

where $\lambda_d^a = \lambda_m + (L_d - L_q)i_d$ is the active flux magnitude masking the saliency. R_s , ω , and p are the stator resistance, the electrical rotor speed, and the differentiate operator, respectively. i_s and u_s are the stator current and voltage. Transformation to the $\alpha\beta$ -reference frame gives

$$u_s^s = R_s i_s^s + pL_q i_s^s + p\lambda_d^{a,s} \quad (3)$$

which on state-space form is equivalent to

$$\begin{bmatrix} u_\alpha \\ u_\beta \end{bmatrix} = \begin{bmatrix} R_s + pL_q & 0 \\ 0 & R_s + pL_q \end{bmatrix} \begin{bmatrix} i_\alpha \\ i_\beta \end{bmatrix} + \begin{bmatrix} e_\alpha \\ e_\beta \end{bmatrix} \quad (4)$$

where e_α and e_β are the equivalent EMF components. These can be represented as

$$\begin{bmatrix} e_\alpha \\ e_\beta \end{bmatrix} = p \begin{bmatrix} \lambda_{da}^a \\ \lambda_{d\beta}^a \end{bmatrix} \simeq w \lambda_d^a \begin{bmatrix} -\sin(\theta) \\ \cos(\theta) \end{bmatrix} \quad (5)$$

where λ_{da}^a and $\lambda_{d\beta}^a$ are the $\alpha\beta$ components of the active flux in the $\alpha\beta$ -reference frame, and θ is the electrical rotor position. In (5), the time derivative of the d current is approximated to zero to simplify the calculations. An approximation, which at steady-state operation is acceptable, but puts demands on the algorithm during transients.

A reasonable approach for state-space representation of (4) and (5) would be to choose a state vector as $[i_\alpha \ i_\beta \ e_\alpha \ e_\beta]^T$, as in [15]. However, the selection of e_α and e_β as states brings unnecessary modeling weakness to the MHE problem. This weakness originates from the inherent magnitude variations of $|e_{\alpha\beta}|$ due to the linear dependence of w as well as the influence of the hidden saliency. The authors instead propose to use a mathematically equivalent model with the state vector defined as

$$x = \begin{bmatrix} i_\alpha \\ i_\beta \\ \frac{\lambda_d^a \cos(\theta)}{L_q} \\ \frac{\lambda_d^a \sin(\theta)}{L_q} \end{bmatrix} = \begin{bmatrix} i_\alpha \\ i_\beta \\ \frac{\lambda_{d,a}^a}{L_q} \\ \frac{\lambda_{d,\beta}^a}{L_q} \end{bmatrix} \quad (6)$$

where the active flux in $\alpha\beta$ coordinates, divided by the q -inductance, were used as states directly. This leads to the following final continuous time state-space matrices:

$$A = \begin{bmatrix} -\frac{R_s}{L_q} & 0 & 0 & \omega \\ 0 & -\frac{R_s}{L_q} & -\omega & 0 \\ 0 & 0 & 0 & -\omega \\ 0 & 0 & \omega & 0 \end{bmatrix} \quad B = \begin{bmatrix} \frac{1}{L_q} & 0 \\ 0 & \frac{1}{L_q} \\ 0 & 0 \\ 0 & 0 \end{bmatrix}, \quad C = \begin{bmatrix} 1 & 0 & 0 & 0 \\ 0 & 1 & 0 & 0 \end{bmatrix}. \quad (7)$$

As can be seen in (7), the only two parameters required are the stator resistance and the q -axis inductance. By incorporating the active flux magnitude in the states, both L_d and λ_m are hidden. Hence, variations in these parameters do not influence the performance of the estimator. Suppressing uncertainties tied to these parameters brings additional robustness to the model which also increases the confidence in the model. Moreover, by including the division by L_q in the two latter states, their magnitude is more comparable to the stator current, which is favorable when solving the MHE problem.

From the estimates \hat{x}_3 and \hat{x}_4 , the rotor position and the rotational speed were obtained using a normalized quadrature phase-locked loop (Q-PLL). The error signal to the Q-PLL was defined as

$$e = 2\hat{x}_3\hat{x}_4 \cos(2\hat{\theta}) - \sin(2\hat{\theta})(\hat{x}_3^2 - \hat{x}_4^2). \quad (8)$$

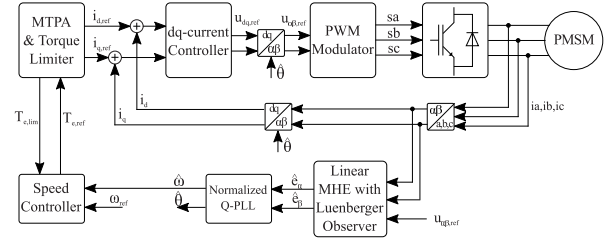


Fig. 2. Illustration of the drive system with discrete-time implementation of the MHE estimator and the cascade coupled speed and dq current controllers.

In the Q-PLL, the rotational speed was obtained by a PI controller driven by the error (8), whereas the rotor angle was obtained by integrating the rotational speed, much in similarity with the proposed Q-PLL presented in [17].

The closed-loop transfer function of the Q-PLL is

$$\frac{\hat{\theta}}{\theta} = \frac{sK_p + K_i}{s^2 + sK_p + K_i}. \quad (9)$$

The poles were defined as complex conjugates and located at $s = (-1 \pm j)\omega_b/\sqrt{2}$, resulting in $K_p = \sqrt{2}\omega_b$ and $K_i = \omega_b^2$, where ω_b is regarded as the bandwidth of the Q-PLL.

An overview of the discrete-time implementation of the controller can be seen in Fig. 2. As can be seen, the dq current reference calculation was based on the maximum torque per ampere approach for energy efficiency purposes. The dq current controller constitutes of two parallel controllers where the d - and q -components were treated separately by the use of feedforward of the coupling terms and the induced voltage. In addition, the controllers were extended with active damping and antiwindup for performance enhancement purposes. Variations in the dq inductances and the flux constant due to magnetic saturation were compensated for online, by the use of lookup tables.

B. Luenberger Observer Extension

In the proposed algorithm, the state-space model, based on discretization of the model in (7), was extended with a Luenberger output feedback observer. Luenberger observers have shown superiority, both considering robustness and performance, in several comparative studies [18], [19]. The observer adds a correction to the model by its feedback of the measurable states to enhance the dynamic performance, primarily at low rotational speeds. The resulting system dynamics was modeled as

$$\begin{aligned} \dot{x} &= Ax + Bu + L(y - \hat{y}) \\ \hat{y} &= Cx \end{aligned} \quad (10)$$

where L is the Luenberger gain matrix, and y and \hat{y} are the measured and estimated phase currents in the $\alpha\beta$ -reference frame.

The pole assignment selection was based on a tradeoff between response time and robustness. In Fig. 3, the poles of the error dynamics are presented for various rotational speeds. The observer gain matrix was designed based on pole assignment of the error dynamics $(A - LC)$, where the

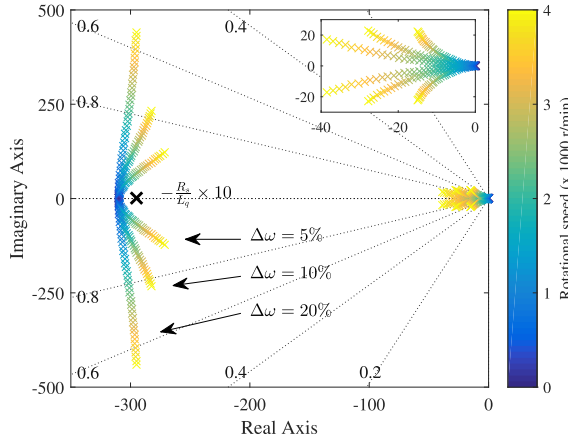


Fig. 3. Poles of closed-loop system dynamics using the Luenberger observer presented for various rotational speeds.

observer dynamics were set to be approximately 10 times faster than that of the system dynamics. As discussed by Zhang *et al.* [19], the pole assignment is a delicate matter in variable speed drive applications. In the proposed algorithm, the gain matrix is derived at a certain rotational speed of the machine and scaled linearly with the speed as it varies. It is of high importance to study, for instance, the root locus for a wide speed range to guarantee observer stability for the entire rotational speed range.

Without the observer, the poles of the system were located at $[-R_s/L_q, -R_s/L_q, j\omega, -j\omega]$. As shown in Fig. 3, the poles for the first two states are around 10 times faster and the poles for the last two states are relocated from the imaginary axis into the left half-plane. Although the Luenberger observer is unable to move the poles away from the origin at zero speed, it improves the attributes at close to zero speed operation. Moreover, Fig. 3 also shows implications of rotor speed estimation error on the observers pole location. A scenario likely to appear during transients. As can be seen, as the error increases the complex conjugated poles move further away from the real axis. Hence, the damping ratio is decreased and the system get less damped. Yet, significant estimation errors do not result in an unstable observer.

Although the Luenberger observer improves low-speed characteristics, it does not remedy the lack of observability occurring at zero speed. Previous research has shown that back EMF observers successfully can be extended with HF signal injection techniques to solve zero-speed operation [10], [20]–[24]. It is believed that HF signal injection likewise can be combined with the proposed method, although it is not within the scope of this paper.

Despite the issue with loss of observability at zero speed, it is shown in Section V that low-speed operation and speed reversal is manageable.

C. Model Discretization

The sinusoidal nature of the states and the input signals requires attention to the selection of discretization method. It is desirable to obtain a reasonably accurate discretization approximation within the limitations of computational power.

Having a zero-order hold element on the input, the trajectory of the state vector over discrete time can be expressed as

$$\begin{aligned} x(k+1) &= A_d x(k) + B_d u(k) \\ y(k) &= C_d x(k) \end{aligned} \quad (11)$$

where

$$A_d = \mathcal{L}^{-1}\{(sI - A)^{-1}\}|_{t=h} = e^{At}|_{t=h} = e^{Ah} \quad (12)$$

$$B_d = \mathcal{L}^{-1}\left\{(sI - A)^{-1} \frac{1}{s} B\right\}\bigg|_{t=h} = \int_0^h e^{At} dt B \quad (13)$$

where \mathcal{L}^{-1} is the inverse Laplace transform and h is the time step size. The intractable matrix exponential and integral involved can be numerically approximated as

$$\begin{aligned} A_d &= I + A \left(Ih + \frac{Ah^2}{2!} + \frac{A^2 h^3}{3!} + \dots \right) \\ &= I + AS \\ B_d &= \left(Ih + \frac{Ah^2}{2!} + \frac{A^2 h^3}{3!} + \dots \right) B \\ &= SB. \end{aligned} \quad (14)$$

With the given approximation, the local truncation error diminishes as more terms are used. Using the first term is equivalent to a standard forward Euler difference, with an approximation error of the first-order ($\epsilon \propto h$). In this paper, the first three terms were used which yields a third-order approximation error. This refinement of the discretization is a key figure for high estimation accuracy at high rotational speeds, where the fundamental frequency is high in relation to the update frequency.

IV. MOVING HORIZON ESTIMATION

Parameter estimation using linear systems with random measurement and process noises are commonly seen. From theory, it follows that the Kalman filter (KF) estimator is the optimal linear estimator if the probability distribution of the noise is known and the system representation is exact. Assumptions which might be motivated by mathematical tractability, yet for many practical problems questionable and possibly erroneous.

The motivation for using MHE, with the framework of KF, is based on the hypothesis to remedy problems associated with the aforementioned imperfections, by exploiting more data recursively.

The optimization variables are the state vector in the state-space model, e.g., the phase current and the active flux in the $\alpha\beta$ -reference frame, and the process noise. The optimization objective is to minimize the least-square error between the measured and estimated phase, i.e., the tracking error of the phase current currents, as well as the process noise. The former is rather intuitive, whereas the latter is needed to prevent the noise to completely dominate. If the noise was not included, it will to a larger extent be used to cancel the error defined by the tracking error.

A. Linear MHE Problem Statement

The system was represented with the following discrete-time linear, time-variant, and state-space model:

$$\begin{aligned}\hat{x}_{k+1} &= A_d \hat{x}_k + B_d u_k + w_k + L(y_k - \hat{y}_k) \\ \hat{y}_k &= C \hat{x}_k + v_k \\ \hat{x}_k &\in \mathbb{X}, \quad w_k \in \mathbb{W}, \quad v_k \in \mathbb{V}\end{aligned}\quad (15)$$

where \mathbb{X} , \mathbb{W} , and \mathbb{V} are constrained. The subscript k index the discrete-time samples in the chronological order. The last term, $L(y_k - \hat{y}_k)$, represents the Luenberger output feedback observer, and w_k and v_k are the process and observation noises at time k . Both w_k and v_k are assumed to be zero-mean noises with the covariance matrices Q_k and R_k , respectively. w_k models disturbances and model inaccuracies whereas v_k models sensor noise in the measurement. By forward simulation, the output data sequence $\{\hat{y}_0^k\}$ can be obtained based on measurements $\{y_0^k\}$, the initial state vector x_0 and its covariance matrix Π_0 and the disturbance sequence $\{w_0^k\}$. The initial state vector of the system x_0 was assumed to be normally distributed with mean \bar{x} and covariance Π_0 .

The optimization problem is formulated as the following set of constrained least-squares problem:

$$\begin{aligned}\phi(x_0, w_k) &= \|x_0 - \bar{x}_0\|_{P_0}^2 \\ &+ \sum_{k=0}^T \|y_k - Cx_k\|_V^2 + \sum_{k=0}^{T-1} \|w_k\|_W^2\end{aligned}\quad (16)$$

subject to (15). The norms were defined as $\|z - \bar{z}\|_A^2 := (z - \bar{z})^T A^T A (z - \bar{z})$ and $V^T V = R^{-1}$, $W^T W = Q^{-1}$, and $P_0^T P_0 = \Pi_0^{-1}$, assuming that the covariance matrices are nonsingular and hence invertible.

With this formulation, the problem size grows with time, since more data is included as time proceeds. The complexity of such problems grows at least linearly with time [25]. To make the problem feasible for real-time implementation the problem size needs to be bounded. This was done by employing a moving horizon approach. The approach is based on a fixed horizon where the problem data is bounded by a number of consecutive sampling instances, equivalent to the length of the horizon. Information not explicitly treated within the window of the optimization horizon is summarized in an arrival cost term, updated sequentially as the fixed horizon is moved forward in time. With the approach of a fixed horizon of length N and an arrival cost, the MHE problem can be redefined as

$$\begin{aligned}\phi(x_k, w_k) &:= \phi_{T-N}(x_0) \\ &+ \sum_{k=T-N}^T \|y_k - Cx_k\|_V^2 + \sum_{k=T-N}^{T-1} \|w_k\|_W^2\end{aligned}\quad (17)$$

where the arrival cost $\phi_{T-N}(x_0, w_k)$ at time $k = T - N$ was defined as

$$\phi_{T-N}(x_k) = \|x_{T-N} - \bar{x}_{T-N}\|_{P_{T-N}}^2 + \phi_{T-N}^* \quad (18)$$

where ϕ_{T-N}^* is the optimal cost to go at time $k = T - N$ [25], leading to the final problem definition

$$\begin{aligned}\phi(x_k, w_k) &:= \|x_{T-N} - \bar{x}_{T-N}\|_{P_{T-N}}^2 \\ &+ \underbrace{\sum_{k=T-N}^T \|y_k - Cx_k\|_V^2 + \sum_{k=T-N}^{T-1} \|w_k\|_W^2}_{\Lambda_k}\end{aligned}\quad (19)$$

The solution to the optimization and hence to the minimization of (19), yields the optimal disturbance sequence $\{w\}_{k=T-N}^{k=T-1}$ and the optimal states sequence $\{x\}_{k=T-N}^{k=T}$. The length of the horizon is directly affecting the results and was treated as a tuning parameter in the MHE formulation. Clearly, as the horizon grows more data is explicitly handled by the optimization and the performance is enhanced with the expense of computational burden. However, as the complexity grows at least linearly with the horizon length, but the returns diminish as the horizon is sufficiently large, the computational cost for increased performance increases rapidly as the horizon is extended beyond a certain level. Rao and Rawlings [26] recommend a horizon length twice the order of the system as a reasonable tradeoff between accuracy and computational burden.

The key of preserving stability and enabling high performance is the approximation of the arrival cost term, and explicitly how discarded data, e.g., data falling out of the horizon, is preserved and used in the optimization [14], [26], [27]. For linear unconstrained optimization, the arrival cost can be explicitly expressed using the KF covariance matrix update formula, in opposition to nonlinear systems where analytical approximations are required [27].

As discussed by Rao and Rawlings [26] for linear systems when inequality constraints are inactive, the arrival cost approximation with the KF covariance matrix update is exact. Hence, a reasonable solution is to approximate the arrival cost for the unconstrained problem. The covariance matrix update is obtained by solving the Riccati equation

$$\begin{aligned}\Pi_T &= Q + A \Pi_{T-1} A^T \\ &- A \Pi_{T-1} C^T (R + C \Pi_{T-1} C^T)^{-1} C \Pi_{T-1} A^T.\end{aligned}\quad (20)$$

The solution to the MHE problem is obtained by solving the Lagrange function associated with (19), which turns out as a root finding problem. The solution, defined by the gradient of the dual feasibility equations ($\nabla \mathcal{L}$) and the gradient of the primal feasibility equations ($G = 0$) [28], is defined as

$$\begin{pmatrix} \nabla \mathcal{L} \\ G \end{pmatrix} = 0. \quad (21)$$

The gradient of the Lagrangian results in a set of matrix equations where the gradients themselves are row vectors, each with a size equal to the number of states, expressed as

$$\begin{aligned}\nabla_{x_0} \mathcal{L} &= r_{x_0} = \nabla_{x_0} \Gamma + \nabla_{x_0} \Lambda_0 - \nabla_{x_0} f_0^T \lambda_1 = 0 \\ \nabla_{x_k} \mathcal{L} &= r_{x_k} = \nabla_{x_k} \Lambda_k - \nabla_{x_k} f_k^T \lambda_{k+1} + \lambda_k = 0 \\ \nabla_{x_N} \mathcal{L} &= r_{x_N} = \nabla_{x_N} \Lambda_N + \lambda_k = 0 \\ \nabla_{w_k} \mathcal{L} &= r_{w_k} = \nabla_{w_k} \Lambda_k - \nabla_{w_k} f_k^T \lambda_{k+1} = 0 \\ \nabla_{\lambda_{k+1}} \mathcal{L} &= r_{\lambda_{k+1}} = x_{k+1} - f_k = 0\end{aligned}\quad (22)$$

where Γ is the arrival cost term, Λ_k is the stage cost at time k , and $f_k = A_d \hat{x}_k + B_d u_k + w_k + L(y - \hat{y}_k)$. For $N = 2$, the solution to the MHE problem is obtained solving the following Karush-Kuhn-Tucker (KKT) system:

$$\begin{bmatrix} E_0 & A_0^T & & & \\ & R_0 & G_0^T & & \\ A_0 & G_0 & & -I & \\ & & -I & Q_1 & A_1^T \\ & & & & R_1 & G_1^T \\ & & & & A_1 & G_1 & & -I \\ & & & & & & -I & Q_2 \end{bmatrix} \begin{bmatrix} x_0 \\ w_0 \\ \lambda_0 \\ x_1 \\ w_1 \\ \lambda_1 \\ x_2 \\ w_2 \end{bmatrix} = \begin{bmatrix} r_{x_0} \\ r_{w_0} \\ r_{\lambda_0} \\ r_{x_1} \\ r_{w_1} \\ r_{\lambda_1} \\ r_{x_2} \\ r_{w_2} \end{bmatrix} \quad (23)$$

where $A_k^T = -\nabla_{x_k} f_k^T \lambda_{k+1}$, $G_k^T = -\nabla_{w_k} f_k^T \lambda_{k+1}$, $E_0 = 2C_d^T V^T V C_d + \Pi_0^{-1} + \Pi_0^{-T}$, $R_k = 2W^T W$, and $Q_k = 2C_d^T V^T V C_d$.

Direct multiple shooting was used to solve the problem online. The structure of the symmetric KKT matrix was exploited, and the solution was derived using LU factorization with forward-backward substitution. The problem as a whole was for each time instance defined and solved online, without the use of any offline calculations—an approach which might not be optimal considering turnaround time. If the states would have been selected differently, the time variations could have been moved to the states resulting in a time-invariant system. In such case, much of the computations leading up to the problem definition could be done offline.

The system dynamics was discretized on a uniform time grid, equally spaced with a time separation equal to the update time of the algorithm. On the time intervals, the inputs were treated as piecewise constants. By analogy with nonlinear MHE, a single newton step was used to solve the problem at each time instance.

B. Active Flux-Based Observer Used for Benchmark

To comparatively evaluate the proposed MHE solution, a well-researched and documented observer solution was used as benchmark. The active flux observer used is presented in [16].

The operational principle is similar to what is used in the proposed MHE-solution. The active flux vector in $\alpha\beta$ was estimated based on stator voltage and current as

$$\lambda_d^{a,s} = \int (u_s^s - R_s i_s + u_{\text{comp}}) dt - L_q i_s^s \quad (24)$$

where u_{comp} is a voltage compensation, driven by the difference between stator flux estimated in $\alpha\beta$ - and in dq -coordinates. As discussed in [16], it improves the performance by suppressing, for example, inverter nonidealities.

An illustration of the active flux observer used is seen in Fig. 4.

V. RESULTS

The proposed MHE sensorless algorithm is tested and evaluated using results from both simulations and experimental testing. The evaluation focuses primarily on dynamic performance, parameter sensitivity and turnaround time (e.g., the execution time required for different solutions). The data

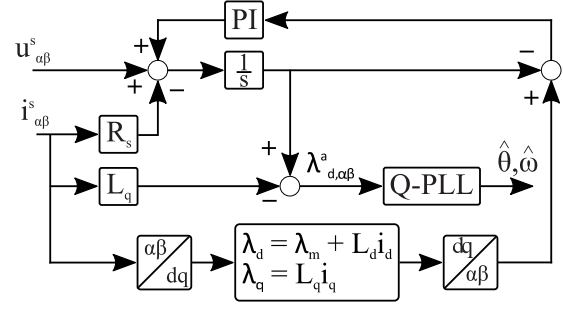


Fig. 4. Illustration of active flux observer used as benchmark for comparative analyses of the proposed MHE solution.

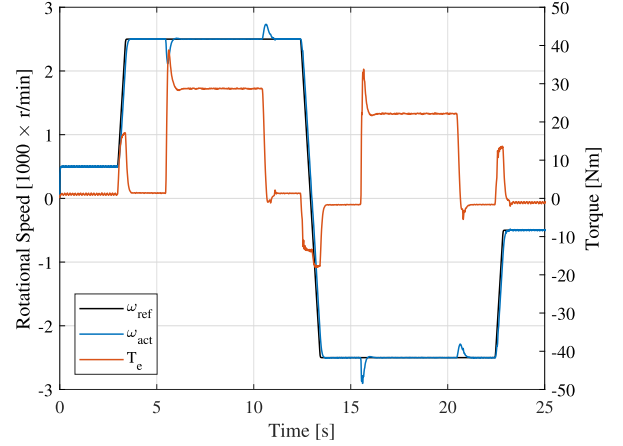


Fig. 5. Speed and torque profiles used during the experimental testing. The measurement procedure was automated to improve consistency when multiple consecutive runs were executed.

were sampled at 4 kHz and has not been post-processed with any kind of filtering. The bandwidth of the speed controller, Q-PLL, and current controllers were 2, 20, and 200 Hz, respectively.

In Fig. 5, the rotational speed and electromagnetic torque profiles used during the experiments are presented. In the first half, both rotational speed and torque are positive, whereas in the second half the speed is reversed while the torque remains positive. Combined, both motor and generator mode as well as positive and negative rotational directions were tested. The speed reversal appears during no load—a case when the system is minimally excited.

In Figs. 6 and 7, the steady-state mean rms error, and the turnaround time are presented for different lengths of the estimation horizon. The mean rms error and its standard deviation were calculated using 40 consecutive measurement series, as the one presented in Fig. 5. The mean rms error was defined as the mean of the rms error in each of the 40 series. As shown in Fig. 6, the MHE solution outperforms the active flux-based observer. Although, it is to a considerable computational cost, as is shown in Fig. 7.

Furthermore, the performance of the MHE is enhanced as the horizon length is extended. However, the benefits of longer horizons decay as it grows. This is clearly in line with previous research where, for instance, Rao and Rawlings [26] recommend a horizon length twice the order of the system as

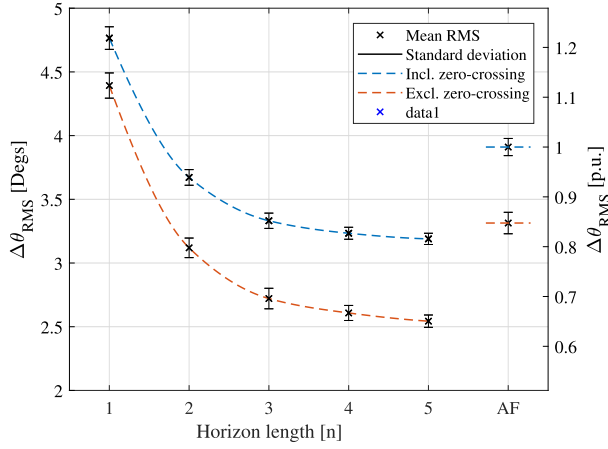


Fig. 6. Measured mean rms error with one standard deviation for MHE with horizon lengths $N = 1-5$ and the active flux observer, each based on 40 measurement series. The results are given both with and without the influence of the zero crossing.

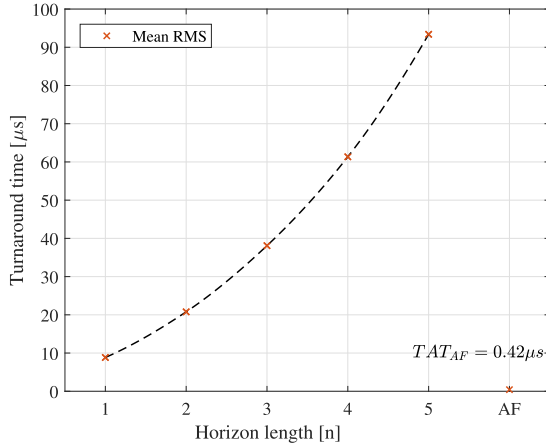


Fig. 7. Measured turnaround time for different horizon lengths as well as for the active flux observer. The results are calculated using 40 measurement series for each setup.

a reasonable tradeoff to reconcile both objectives of performance and turnaround time. The performance enhancements obtained from a longer horizon is not only in terms of mean rms error, it is also shown that the standard deviation decay with longer horizons. A result, showing on increased consistency, which is interpreted as decreased noise sensitivity.

Moreover, it might be appealing to accredit the MHE performance advantage to specific parts of the measurement series. Such as either the zero-crossing event or the other parts. However, as can be seen in Fig. 6, excluding the zero-crossing event data, the absolute values decrease but the trend remains. Clearly, the MHE with a horizon of 2 or longer yields lower rms error than the benchmark solution.

The mean rms rotor position error, its standard deviation and the turnaround time is also summarized in Table II. The data are including the zero-crossing event.

Since none of the solutions are rotor position estimator, but rather active flux estimators, the subsequent Q-PLL is a key factor in both solutions. In Fig. 8, the rotor position error in electrical degrees are presented for different Q-PLL bandwidths.

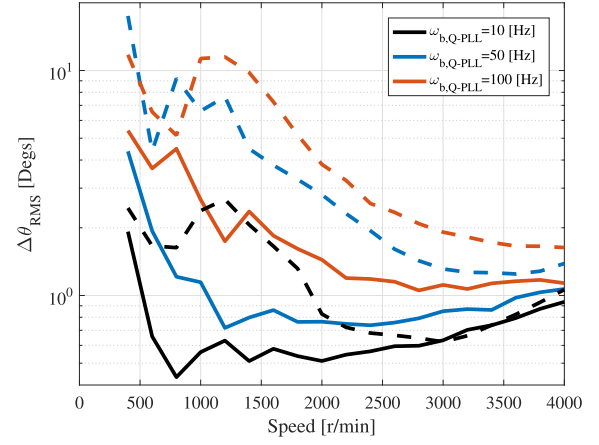


Fig. 8. Measured rms error of rotor position in electrical degrees for different bandwidths of the Q-PLL. The solid and dashed lines show results using MHE and active flux observer, respectively. Each data point is based on steady-state measurements with a duration of 20 s.

TABLE II

ESTIMATION ERROR, STANDARD DEVIATION, AND TURNAROUND TIME FOR DIFFERENT HORIZON LENGTHS

Horizon length	Mean RMS-error [Degs]	Standard dev. [Degs]	TAT [μ s]
MHE (N=1)	4.77 (+21.9%)	0.177 (+31.7%)	8.8
MHE (N=2)	3.67 (−6.1%)	0.123 (−8.8%)	20.8
MHE (N=3)	3.33 (−14.8%)	0.120 (−11.0%)	38.1
MHE (N=4)	3.23 (−17.3%)	0.094 (−30.2%)	61.3
MHE (N=5)	3.19 (−18.4%)	0.088 (−34.6%)	93.4
Active flux-obs.	3.91 ($\pm 0\%$)	0.135 ($\pm 0\%$)	0.4

The data are showing the rms error during no load obtained from 20 second steady-state measurements at every 200 r/min, stretching from 400 to 4000 r/min. At speeds less than 3000 r/min, the difference is significant, hence the logarithmic y-scale. Evidently, the no load performance of the MHE is superior to the reference active flux observer. Although it is not shown, it has been noted (and indicated by the trends in Fig. 8), that stability is kept further toward zero speed for the MHE observer, then for the active flux observer. Furthermore, the MHE solution performs reasonably well with all three Q-PLL bandwidths.

In Figs. 9 and 10, the influence of erroneous q inductance estimates is shown for the MHE- and the active flux-based solutions, respectively. As can be seen, both solutions are more sensitive, in absolute numbers, to overestimating the q -inductance than underestimation. Yet, the most interesting is that both solutions perform reasonably well, even with an error of $\pm 20\%$ —a level which is believed to be well within the limits in most applications. Although, a difference can be seen during the speed zero crossing where the error when using the MHE tends more to zero.

Further parameter sensitivity analyses can be done for the reference estimator. However, due to the lack of d -axis flux in the proposed MHE-solution, analyzing effects of parameter deviation in the d -axis inductance and the magnet flux constant is deemed excessive.

Yet, the fact that their influence is none existing, is considered a significant strength. Particularly for the given

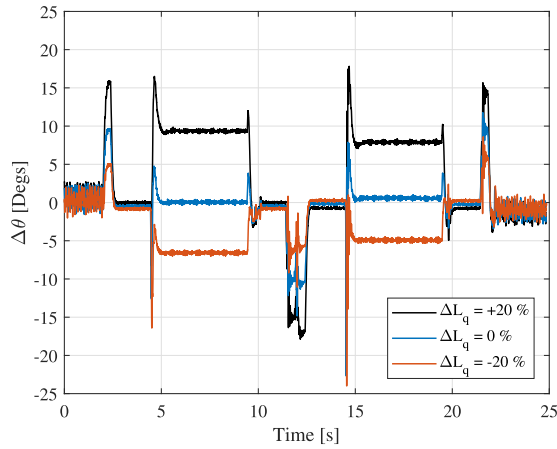


Fig. 9. Measured rotor position error in electrical degrees using the MHE ($N = 5$) with estimation error in the q -inductance.

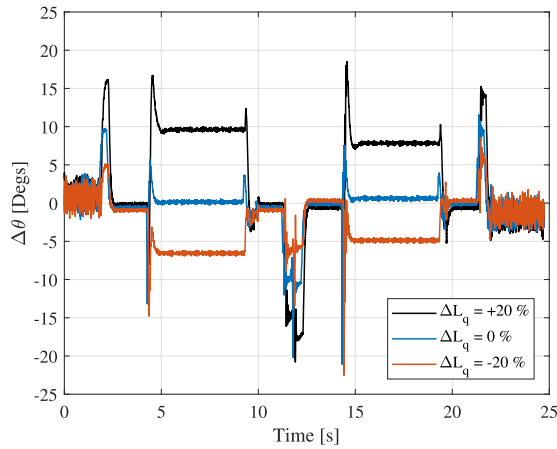


Fig. 10. Measured rotor position error in electrical degrees using the active flux observer with estimation error in the q -inductance.

application, where large temperature variations can be expected. A remark that is clearly in line with the temperature influence investigations presented by Li *et al.* [29], [30]. Investigations, that were conducted with a similar type of IPMSM used for vehicle propulsion, concluding that the d -axis flux is more temperature sensitive than the q -axis flux.

Conclusively, it turns the proposed MHE-solution into a robust universal solution for any synchronous motor, regardless of whether a PM, PM-assisted, or reluctance motor is used, nondependent on the presence of magnetic saliency.

In Figs. 11 and 12, the simulation results of the rotor position estimation error using the MHE-solution are presented for overestimation and underestimation of the d -axis inductance and stator resistance, respectively. Comparing Figs. 11 and 12, it is evident that, for the given intervals ($\pm 20\%$), the influence of errors in the stator resistance is rather negligible in comparison to the q -axis inductance. This difference indicates that, for estimation accuracy purposes, efforts should be spent on the accuracy of the inductance, rather than the stator resistance.

An interesting observation is that the error dynamics changes in the field weakening region, and for the inductance the error decreases with increased rotational speed. This is

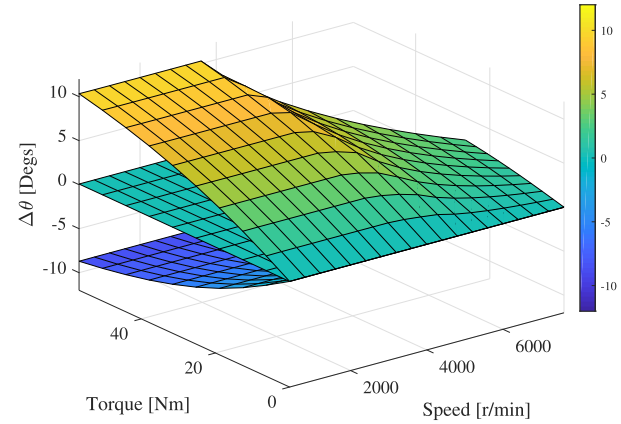


Fig. 11. Simulated steady-state estimation error of rotor angle in electrical degrees for $\Delta L_q = -20\%$ (lower), $\Delta L_q = 0\%$ (middle), and $\Delta L_q = +20\%$ (upper), using the MHE solution with $N = 5$.

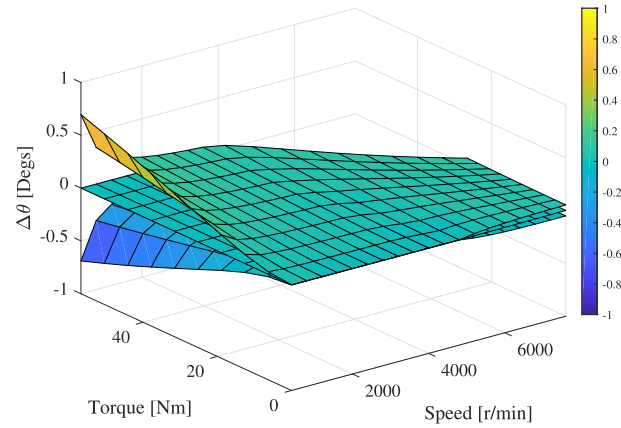


Fig. 12. Simulated steady-state estimation error of rotor angle in electrical degrees for $\Delta R_s = -20\%$ (lower), $\Delta R_s = 0\%$ (middle), and $\Delta R_s = +20\%$ (upper), using the MHE-solution with $N = 5$.

believed to be due to the active flux magnitude decrease, as the d current becomes more negative. As the magnitude of the active flux becomes less significant, the algorithm does not need to utilize these terms to compensate for the remain errors in the state-space representation. Similarly, as the phase current magnitude is increased, the influence of the accuracy of the stator resistance is increased.

Next, rapid transients are investigated. In Figs. 13–17, the results from a step response in the torque, from no load to rated torque, are shown. The fluctuations seen in the dq current references in the time interval from 0.25 to 0.35 are due to peak torque limits which decrease as the rotational speed briefly exceed the base speed. Note that the momentary dc voltage drop momentarily reduces the rated speed below the indicated values in Table I. This also shows both solutions abilities and stability at rated torque and speed. Moreover, the large-magnitude and low-frequency (16.7 Hz) oscillations seen in all data is due to the response of the (thyristor) rectifier and speed controlled dc machine used as load.

As can be seen in Figs. 13–17, both solutions perform well with rapid reference changes. In Fig. 17, showing the q current characteristics, the time axis is enlarged around the reference

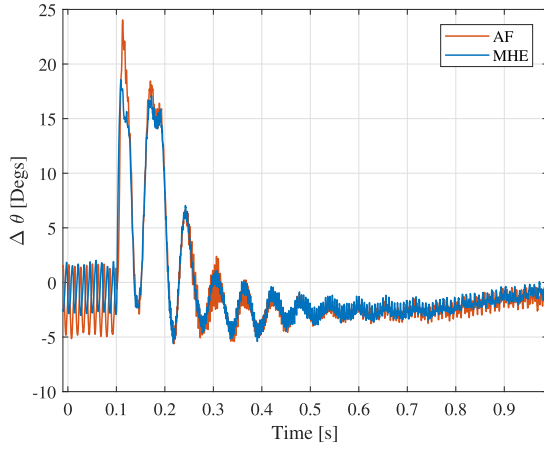


Fig. 13. Measured rotor position error in electrical degrees using the MHE ($N = 5$) and the active-flux reference observer (AF) during load torque step from no load to rated torque at 1000 r/min.

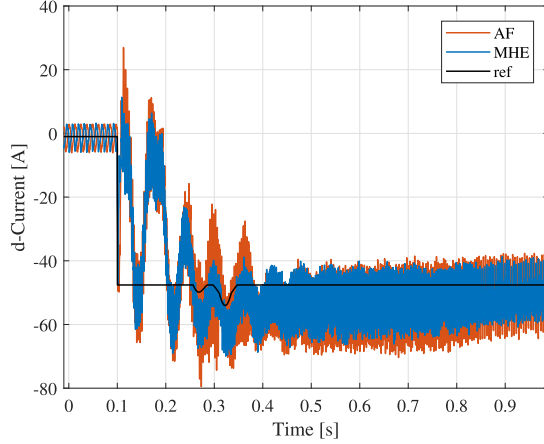


Fig. 14. Measured d current error using the MHE ($N = 5$) and the active-flux reference observer (AF) during load torque step from no load to rated torque at 1000 r/min.

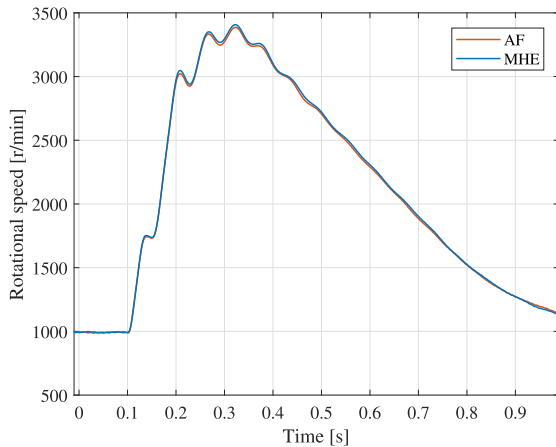


Fig. 15. Measured rotational speed in mechanical r/min using the MHE ($N = 5$) and the active-flux reference observer (AF) during load torque step from no load to rated torque at 1000 r/min.

step to show a more detailed view of the step response. As can be seen, the rise time is approximately $1 \mu s$ which by far exceeds the needs for the intended application.

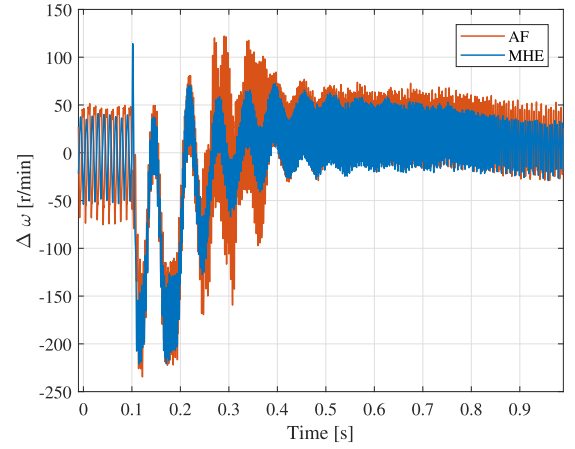


Fig. 16. Measured rotational speed error in electrical r/min using the MHE ($N = 5$) and the active-flux reference observer (AF) during load torque step from no load to rated torque at 1000 r/min.

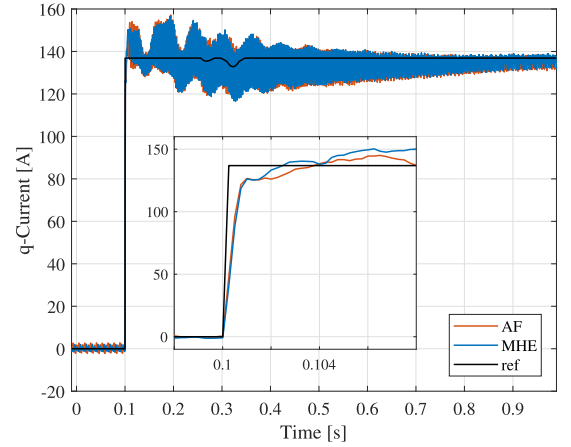


Fig. 17. Measured q current error using the MHE ($N = 5$) and the active-flux reference observer (AF) during load torque step from no load to rated torque at 1000 r/min.

VI. CONCLUSION

An MHE algorithm for motion sensorless control of an IPMSM is presented in this paper. A detailed analysis of its performance is given, in relation to a well-established active flux-based observer.

It is shown that the proposed solution is feasible, that the associated dynamic optimization problem can be solved in real-time, while exploiting the attractiveness of the MHE-approach to obtain highly accurate estimates.

The influence of the length of the estimation horizon is discussed. It is shown that the length of the horizon directly affects the performance, where longer horizons are preferable. Although, it comes with an increasing computational cost.

Moreover, the absence of d -axis flux in the proposed solution is considered a significant strength. Conclusively, it turns the proposed solution into a universal solution for any synchronous motor, regardless of whether a PM, PM-assisted, or reluctance motor is used, nondependent on the presence of magnetic saliency.

REFERENCES

- [1] W. Zine *et al.*, "Compensation of cross-saturation effects on IPMSM sensorless control—Application to electric vehicle," in *Proc. 42nd Annu. Conf. IEEE Ind. Electron. Soc. (IECON)*, Oct. 2016, pp. 6675–6680.

- [2] B. Sarlioglu, C. T. Morris, D. Han, and S. Li, "Benchmarking of electric and hybrid vehicle electric machines, power electronics, and batteries," in *Proc. Int. Aegean Conf. Electr. Mach. Power Electron. (ACEMP)*, Sep. 2015, pp. 519–526.
- [3] S.-K. Sul, Y.-C. Kwon, and Y. Lee, "Sensorless control of IPMSM for last 10 years and next 5 years," *CES Trans. Elect. Mach. Syst.*, vol. 1, no. 2, pp. 91–99, 2017.
- [4] I. Boldea and S. C. Agarlita, "The active flux concept for motion-sensorless unified AC drives: A review," in *Proc. Int. Aegean Conf. Electr. Mach. Power Electron. Electromotion Joint Conf. (ACEMP)*, Sep. 2011, pp. 1–16.
- [5] I. Boldea, M. C. Paicu, and G. D. Andreescu, "Active flux concept for motion-sensorless unified AC drives," *IEEE Trans. Power Electron.*, vol. 23, no. 5, pp. 2612–2618, Sep. 2008.
- [6] S. Rind, Y. Ren, and L. Jiang, "Traction motors and speed estimation techniques for sensorless control of electric vehicles: A review," in *Proc. 49th Int. Univ. Power Eng. Conf. (UPEC)*, Sep. 2014, pp. 1–6.
- [7] R. Bojoi, M. Pastorelli, J. Bottomley, P. Giangrande, and C. Gerada, "Sensorless control of PM motor drives—A technology status review," in *Proc. IEEE Workshop Electr. Mach. Design, Control Diagnosis (WEMDCD)*, Mar. 2013, pp. 168–182.
- [8] S. Chi, Z. Zhang, and L. Xu, "Sliding-mode sensorless control of direct-drive PM synchronous motors for washing machine applications," *IEEE Trans. Ind. Appl.*, vol. 45, no. 2, pp. 582–590, Mar. 2009.
- [9] S. Ichikawa, M. Tomita, S. Doki, and S. Okuma, "Sensorless control of permanent-magnet synchronous motors using online parameter identification based on system identification theory," *IEEE Trans. Ind. Electron.*, vol. 53, no. 2, pp. 363–372, Apr. 2006.
- [10] A. Yousefi-Talouki, P. Pescetto, G. Pellegrino, and I. Boldea, "Combined active flux and high-frequency injection methods for sensorless direct-flux vector control of synchronous reluctance machines," *IEEE Trans. Power Electron.*, vol. 33, no. 3, pp. 2447–2457, Mar. 2018.
- [11] Y. Lee, Y.-C. Kwon, and S.-K. Sul, "Comparison of rotor position estimation performance in fundamental-model-based sensorless control of PMSM," in *Proc. IEEE Energy Convers. Congr. Expo. (ECCE)*, Sep. 2015, pp. 5624–5633.
- [12] R. Kumar, S. Das, P. Syam, and A. K. Chattopadhyay, "Review on model reference adaptive system for sensorless vector control of induction motor drives," *IET Electr. Power Appl.*, vol. 9, no. 7, pp. 496–511, 2015.
- [13] D. Frick, A. Domahidi, M. Vukov, S. Mariéthoz, M. Diehl, and M. Morari, "Moving horizon estimation for induction motors," in *Proc. IEEE Symp. Sensorless Control Elect. Drives (SLED)*, Sep. 2012, pp. 1–6.
- [14] P. Kühl, M. Diehl, T. Kraus, J. P. Schlöder, and H. G. Bock, "A real-time algorithm for moving horizon state and parameter estimation," *Comput. Chem. Eng.*, vol. 35, no. 1, pp. 71–83, Jan. 2011.
- [15] Z. Guoqiang, W. Gaolin, N. Ronggang, and X. Dianguo, "Active flux based full-order discrete-time sliding mode observer for position sensorless IPMSM drives," in *Proc. 17th Int. Conf. Elect. Mach. Syst. (ICEMS)*, Oct. 2014, pp. 3569–3572.
- [16] F. J. H. Kalluf, A. S. Isfănuți, L. N. Tutelea, A. Moldovan-Popa, and I. Boldea, "1-kW 2000–4500 r/min ferrite PMSM drive: Comprehensive characterization and two sensorless control options," *IEEE Trans. Ind. Appl.*, vol. 52, no. 5, pp. 3980–3989, Sep. 2016.
- [17] Y. Zhang and J. Liu, "An improved Q-PLL to overcome the speed reversal problems in sensorless PMSM drive," in *Proc. IEEE 8th Int. Power Electron. Motion Control Conf. (IPEMC-ECCE Asia)*, May 2016, pp. 1884–1888.
- [18] L. Saihi and A. Bouter, "Robust sensorless sliding mode control of pmsm with mras and luenberger extended observer," in *Proc. 8th Int. Conf. Modeling, Identificat. Control (ICMIC)*, Nov. 2016, pp. 174–179.
- [19] X. Zhang, G. Tian, Y. Huang, and Z. Lu, "A comparative study of pmsm sensorless control algorithms: Model based vs luenberger observer," in *Proc. IEEE Veh. Power Propulsion Conf. (VPPC)*, Oct. 2016, pp. 1–6.
- [20] A. Piippo and J. Luomi, "Adaptive observer combined with HF signal injection for sensorless control of PMSM drives," in *Proc. IEEE Int. Conf. Electr. Mach. Drives*, May 2005, pp. 674–681.
- [21] O. Wallmark and L. Harnefors, "Sensorless control of salient PMSM drives in the transition region," *IEEE Trans. Ind. Electron.*, vol. 53, no. 4, pp. 1179–1187, Jun. 2006.
- [22] G.-D. Andreescu, C. I. Pitic, F. Blaabjerg, and I. Boldea, "Combined flux observer with signal injection enhancement for wide speed range sensorless direct torque control of IPMSM drives," *IEEE Trans. Energy Convers.*, vol. 23, no. 2, pp. 393–402, Jun. 2008.
- [23] F. J. W. Barnard, W. T. Villet, and M. J. Kamper, "Hybrid active-flux and arbitrary injection position sensorless control of reluctance synchronous machines," *IEEE Trans. Ind. Appl.*, vol. 51, no. 5, pp. 3899–3906, Sep. 2015.
- [24] A. Yousefi-Talouki, P. Pescetto, and G. Pellegrino, "Sensorless direct flux vector control of synchronous reluctance motors including standstill, MTPA, and flux weakening," *IEEE Trans. Ind. Appl.*, vol. 53, no. 4, pp. 3598–3608, Jul. 2017.
- [25] C. V. Rao, J. B. Rawlings, and J. H. Lee, "Constrained linear state estimation—A moving horizon approach," *Automatica*, vol. 37, no. 10, pp. 1619–1628, 2001.
- [26] C. V. Rao and J. B. Rawlings, "Constrained process monitoring: Moving-horizon approach," *AIChE J.*, vol. 48, no. 1, pp. 97–109, 2002.
- [27] C. C. Qu and J. Hahn, "Computation of arrival cost for moving horizon estimation via unscented Kalman filtering," *J. Process Control*, vol. 19, no. 2, pp. 358–363, 2009.
- [28] S. Boyd and L. Vandenberghe, *Convex Optimization*. Cambridge, U.K.: Cambridge Univ. Press, 2004.
- [29] S. Li, B. Sarlioglu, S. Jurkovic, N. R. Patel, and P. Savagian, "Analysis of temperature effects on performance of interior permanent magnet machines for high variable temperature applications," *IEEE Trans. Ind. Appl.*, vol. 53, no. 5, pp. 4923–4933, Oct. 2017.
- [30] S. Li, B. Sarlioglu, S. Jurkovic, N. Patel, and P. Savagian, "Analysis of temperature effects on performance of interior permanent magnet machines," in *Proc. IEEE Energy Convers. Congr. Expo. (ECCE)*, Sep. 2016, pp. 1–8.



Andreas Andersson (S'14) was born in Gothenburg, Sweden in 1988. He received the B.S. and M.S. degrees in electrical engineering and electric power engineering from the Chalmers University of Technology, Gothenburg, Sweden, in 2010 and 2013, respectively. He is currently pursuing the Ph.D. degree with the Division of Electric Power Engineering, Chalmers University of Technology and also with the Department of Electric Propulsion Systems, Volvo Car Group, Gothenburg.

His current research interests include electric drives and controls.



Torbjörn Thiringer (S'93–M'96–SM'13) received the M.S. and Ph.D. degrees from the Chalmers University of Technology, Gothenburg, Sweden, in 1989 and 1996, respectively.

He is currently a Professor in applied power electronics with the Chalmers University of Technology. His current research interests include the modeling, control and grid integration of wind energy converters into power grids as well as power electronics, and drives for automotive applications.